Scaling properties of saddle-node bifurcations on fractal basin boundaries

Romulus Breban,[1] Helena E. Nusse,[2,*] and Edward Ott[1,†]

[1]*Department of Physics, Institute for Research in Electronics and Applied Physics, University of Maryland, College Park, MD 20742*
[2]*Institute for Physical Sciences and Technology, University of Maryland, College Park, Maryland 20742, USA*

We analyze situations where a saddle-node bifurcation occurs on a fractal basin boundary. Specifically, we are interested in what happens when a system parameter is slowly swept in time through the bifurcation. Such situations are known to be indeterminate in the sense that it is difficult to predict the eventual fate of an orbit that tracks the prebifurcation node attractor as the system parameter is swept through the bifurcation. In this paper we investigate the scaling of (1) the fractal basin boundary of the static (i.e., unswept) system near the saddle-node bifurcation, (2) the dependence of the orbit's final destination on the sweeping rate, (3) the dependence of the time it takes for an attractor to capture a swept orbit on the sweeping rate, and (4) the dependence of the final attractor capture probability on the noise level. With respect to noise, our main result is that the effect of noise scales with the 5/6 power of the parameter drift rate. Our approach is to first investigate all these issues using one-dimensional map models. The simplification of treatment inherent in one dimension greatly facilitates analysis and numerical experiment, aiding us in obtaining the new results listed above. Following our one-dimensional investigations, we explain that these results can be applied to two-dimensional systems. We show, through numerical experiments on a periodically forced second-order differential equation example, that the scalings we have found also apply to systems that result in two-dimensional maps.

PACS number(s): 05.45.Df, 02.30.Oz

I. INTRODUCTION

It is common for dynamical systems to have two or more coexisting attractors. In predicting the long-term behavior of such a system, it is important to determine sets of initial conditions of orbits that approach each attractor (i.e., the basins of attraction). The boundaries of such sets are often fractal ([1], Chap. 5 of [2], and references therein). The fine-scale fractal structure of such a boundary implies increased sensitivity to errors in the initial conditions: Even a considerable decrease in the uncertainty of initial conditions may yield only a relatively small decrease in the probability of making an error in determining in which basin such an initial condition belongs [1,2]. For a discussion of fractal basin boundaries in experiments, see Chap. 14 of [3].

Thompson and Soliman [4] showed that another source of uncertainty induced by fractal basin boundaries may arise in situations in which there is slow (adiabatic) variation of the system. For example, consider a fixed-point attractor of a map (a node). As a system parameter varies slowly, an orbit initially placed on the node attractor moves with time, closely following the location of the solution for the fixed point in the absence of the temporal parameter variation. As the parameter varies, the node attractor may suffer a saddle-node bifurcation. For definiteness, say that the node attractor exists for values of the parameter μ in the range $\mu < \mu_*$ and that the saddle-node bifurcation of the node occurs at μ

$= \mu_*$. Now assume that, for a parameter interval $[\mu_L, \mu_R]$ with $\mu_L < \mu_* < \mu_R$, in addition to the node, there are also two other attractors A and B and that the boundary of the basin of attractor A, attractor B, and the node is a fractal basin boundary. We are interested in the typical case where, before the bifurcation, the saddle lies on the fractal basin boundary, and thus, at the bifurcation, the merged saddle-node orbit is on the basin boundary. In such a case an arbitrarily small ball about the saddle node at $\mu = \mu_*$ contains pieces of the basins of both A and B. Thus, as μ slowly increases through μ_*, it is unclear whether the orbit following the node will go to A or to B after the node attractor is destroyed by the bifurcation. In practice, noise or round-off error may lead the orbit to go to one attractor or the other, and the result can often depend very sensitively on the specific value of the slow rate at which the system parameter varies.

We note that the study of orbits swept through an indeterminate saddle-node bifurcation belongs to the theory of dynamical bifurcations. Many authors have analyzed orbits swept through other bifurcations, like the period doubling bifurcation [5], the pitchfork bifurcation [6,7], and the transcritical bifurcation [7]. In all these studies of the bifurcations listed above, the local structure before *and* after the bifurcation includes stable invariant manifolds varying smoothly with the bifurcation parameter (i.e., a stable fixed point that exists before or after the bifurcation and whose location varies smoothly with the bifurcation parameter). This particular feature of the local bifurcation structure, not shared by the saddle-node bifurcation, allows for well-posed, locally defined problems of dynamical bifurcations. The static saddle-node bifurcation has received much attention in theory and experiments [8–10], but so far, no dynamical

_____

*Permanent address: Department of Econometrics, University of Groningen, P.O. Box 800, NL-9700 AV, Groningen, The Netherlands.

†Also at Department of Electrical and Computer Engineering, University of Maryland, College Park, MD 20742.

bifurcation problems have been defined for the saddle-node bifurcation. In this work, we demonstrate that, in certain common situations, global structure (e.g., an invariant Cantor set or a fractal basin boundary) adds to the local properties of the saddle-node bifurcation and allows for well-posed problems of dynamical bifurcations.

Situations where a saddle-node bifurcation occurs on a fractal basin boundary have been studied in two-dimensional Poincaré maps of damped forced oscillators [4,11,12]. Several examples of such systems are known [4,12], and it seems that this is a common occurrence in dynamical systems. In this work, we first focus on saddle-node bifurcations that occur for one-parameter families of smooth one-dimensional maps having multiple critical points (a critical point is a point at which the derivative of the map vanishes). Since one-dimensional dynamics is simpler than two-dimensional dynamics, indeterminate bifurcations can be more simply studied, without the distraction of extra mathematical structure. Taking advantage of this, we are able to efficiently investigate several scaling properties of these bifurcations. In particular, we investigate the scaling of (1) the fractal basin boundary of the static (i.e., unswept) system near the saddle-node bifurcation (Secs. II B and II C), (2) the dependence of the orbit final destination on the sweeping rate (Sec. II D), (3) the dependence of the time it takes for an attractor to capture the swept orbit following the bifurcation on the sweeping rate (Sec. II E), and (4) the dependence of the final attractor capture probability on the noise level (Sec. II F). Following our one-dimensional investigations, we explain that these results apply to two-dimensional systems. We show, through numerical experiments on the periodically forced Duffing oscillator, that the scalings we have found also apply to higher-dimensional systems (Sec. III).

For one-dimensional maps, a situation dynamically similar to that in which there is indeterminacy in which attractor captures the orbit can also occur in cases where there are two rather than three (or more) attractors (Sec. IV). In particular, we can have the situation where one attractor persists for all values of the parameters we consider and the other attractor is a node which is destroyed via a saddle-node bifurcation on the basin boundary separating the basins of the two attractors. In such a situation, an orbit starting on the node and swept through the saddle-node bifurcation will go to the remaining attractor. It is possible to distinguish different ways that the orbit initially on the node approaches the remaining attractor. We find that the way in which this attractor is approached can be indeterminate.

II. INDETERMINACY IN WHICH ATTRACTOR IS APPROACHED

We consider the general situation of a one-dimensional real map $f_\mu(x)$ depending on a parameter μ. We assume the following: (1) the map is twice differentiable with respect to x and once differentiable with respect to μ (the derivatives are continuous), (2) f_μ has at least two attractors sharing a fractal basin boundary for parameter values in the vicinity of μ_*, and (3) an attracting fixed point x_* of the map $f_\mu(x)$ is destroyed by a saddle-node bifurcation as the parameter μ
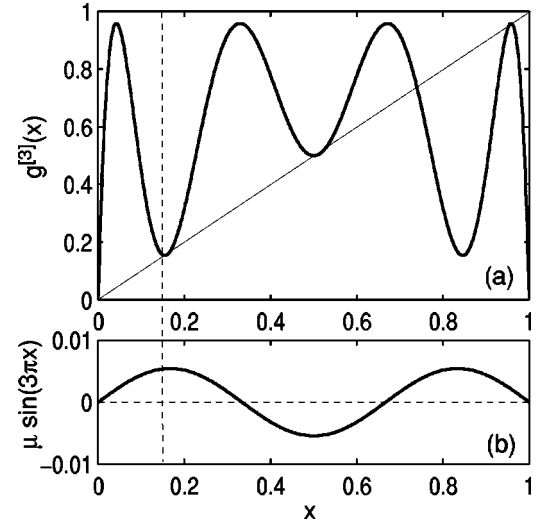

FIG. 1. Construction of the function $f_\mu(x)$ starting with (a) the third iterate of the logistic map, $g(x) = rx(1-x)$, with $r = 3.832$, and adding a perturbation (b) $\mu \sin(3\pi x)$ ($\mu = 5.4 \times 10^{-3}$).

increases through a critical value μ_*, and this saddle-node bifurcation occurs on the common boundary of the basins of the two attractors.

We first recall the saddle-node bifurcation theorem (see, for example, [8]). If the map $f_\mu(x)$ satisfies (a) $f_{\mu_*}(x_*) = x_*$, (b) $(\partial f_{\mu_*}/\partial x)(x_*) = 1$, (c) $(\partial^2 f_{\mu_*}/\partial^2 x)(x_*) > 0$, and (d) $(\partial f/\partial \mu)(x_*; \mu_*) > 0$, then the map f_μ undergoes a backward saddle-node bifurcation (i.e., the node attractor is destroyed at x_* as μ increases through μ_*). If the inequality in either (c) or (d) is reversed, then the map undergoes a forward saddle-node bifurcation, while if both these inequalities are reversed, the bifurcation remains backward. A saddle-node bifurcation in a one-dimensional map is also called a tangent or a fold bifurcation.

A. Model

As an illustration of an indeterminate saddle-node bifurcation in a one-dimensional map, we construct an example in the following way. We consider the logistic map for a parameter value where there is a stable period three orbit. We denote this map $g(x)$ and its third iterate $g^{[3]}(x)$. The map $g^{[3]}(x)$ has three stable fixed points. We perturb the map $g^{[3]}(x)$ by adding a function (which depends on a parameter μ) that will cause a saddle-node bifurcation of one of the attracting fixed points but not of the other two [see Figs. 1(a) and 1(b)]. We investigate

$$f_\mu(x) = g^{[3]}(x) + \mu \sin(3\pi x),$$

$$\text{where} \quad g(x) = 3.832x(1-x). \quad (1)$$

Numerical calculations show that the function $f_\mu(x)$ satisfies all the conditions of the saddle-node bifurcation theorem for having a backward saddle-node bifurcation at $x_* \approx 0.159\,70$ and $\mu_* \approx 0.002\,79$. Figure 2(a) displays how the basins of the three attracting fixed points of the map f_μ change with variation of μ. For $\mu = 0$ the third iterate of the logistic map
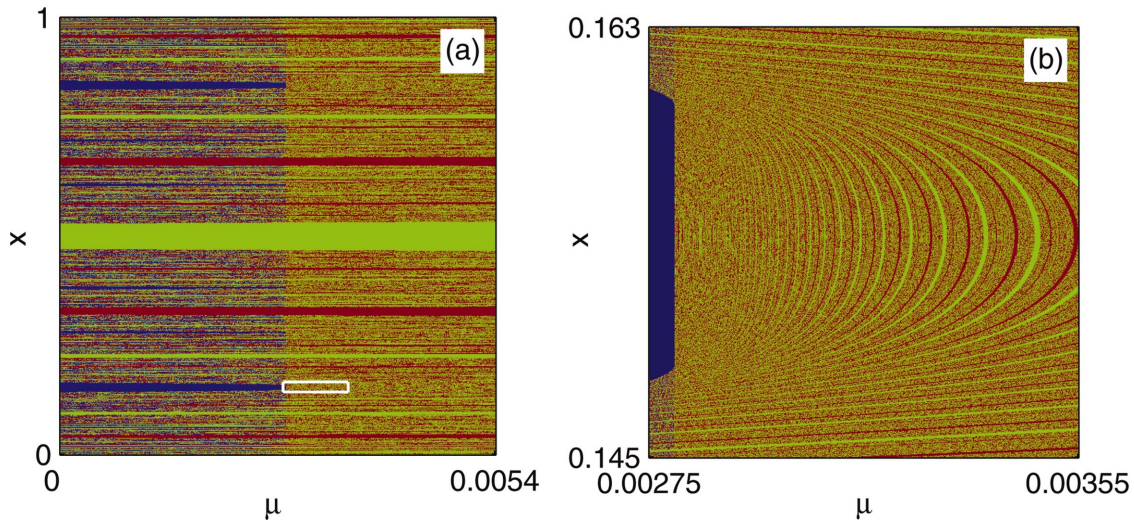
FIG. 2. (Color) (a) Basin structure of the map f_μ versus the parameter μ on the horizontal axis. The attractor having the blue basin is destroyed at $\mu \approx 2.79 \times 10^{-3}$. (b) Detail of the region shown as the white rectangle in (a).

is unperturbed, and it has three attracting fixed points whose basins we color coded with blue, green, and red. For every value of μ, the red region $R[\mu]$ is the set of initial conditions attracted to the rightmost stable fixed point which we denote R_μ. The green region $G[\mu]$ is the set of initial conditions attracted to the middle stable fixed point which we denote G_μ. The blue region $B[\mu]$ is the set of initial conditions attracted to the leftmost stable fixed point which we denote B_μ.

For $\mu < \mu_*$, each of these colored sets has infinitely many disjoint intervals and a fractal boundary. As μ increases, the leftmost stable fixed point B_μ is destroyed via a saddle-node bifurcation on the fractal basin boundary. In fact, in this case, for $\mu < \mu_*$, every boundary point of one basin is a boundary point for all three basins. (That is, an arbitrarily small x interval centered about any point on the boundary of any one of the basins contains pieces of the other two basins.) The basins are so-called Wada basins [13]. This phenomenon of a saddle-node bifurcation on the fractal boundary of Wada basins also occurs for the damped forced oscillators studied in Refs. [11,12]. Alternatively, if we look at the saddle-node bifurcation as μ decreases through the value μ_*, then the basin $B[\mu]$ of the newly created stable fixed point immediately has infinitely many disjoint intervals and its boundary displays fractal structure. According to the terminology of Robert *et al.* [14], we may consider this bifurcation an example of an "explosion."

B. Dimension of the fractal basin boundary

Figure 3 graphs the computed dimension D of the fractal basin boundary versus the parameter μ. For $\mu < \mu_*$, we observe that D appears to be a continuous function of μ. Park *et al.* [15] argue that the fractal dimension of the basin boundary near μ_*, for $\mu < \mu_*$, scales as

$$D(\mu) \approx D_* - k(\mu_* - \mu)^{1/2}, \qquad (2)$$

with D_* the dimension at $\mu = \mu_*$ (D_* is less than the dimension of the phase space) and k a positive constant. Figure

3 shows that the boundary dimension D experiences a discontinuous jump at the saddle-node bifurcation when $\mu = \mu_*$. We believe that this is due to the fact that the basin $B[\mu]$ suddenly disappears for $\mu > \mu_*$.

The existence of a fractal basin boundary has important practical consequences. In particular, for the purpose of determining which attractor eventually captures a given orbit, the arbitrarily fine-scaled structure of fractal basin boundaries implies considerable sensitivity to small errors in initial conditions. If we assume that initial points cannot be located more precisely than some $\epsilon > 0$, then we cannot determine which basin a point is in, if it is within ϵ of the basin boundary. Such points are called ϵ uncertain. The Lebesgue measure of the set of ϵ-uncertain points (in a bounded region of interest) scales like $\epsilon^{D_0 - D}$, where D_0 is the dimension of the phase space ($D_0 = 1$ for one-dimensional maps) and D is the box-counting dimension of the basin boundary [1]. For the case of a fractal basin boundary, $(D_0 - D) < 1$. When $D_0 - D$ is small, a large decrease in ϵ results in a relatively

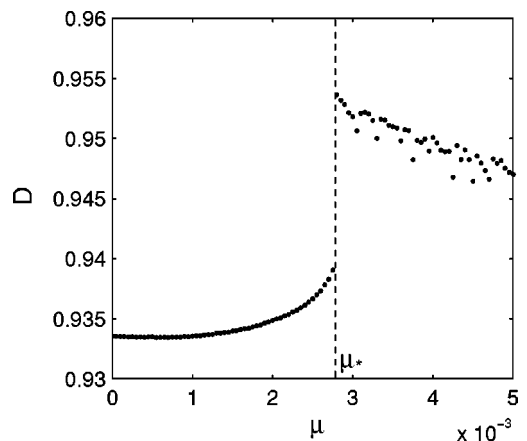FIG. 3. Fractal dimension of the basin boundary versus μ. Notice the continuous variation for $\mu < \mu_*$ and the discontinuous jump at μ_*, the parameter value at which the saddle-node bifurcation on the fractal basin boundary takes place.
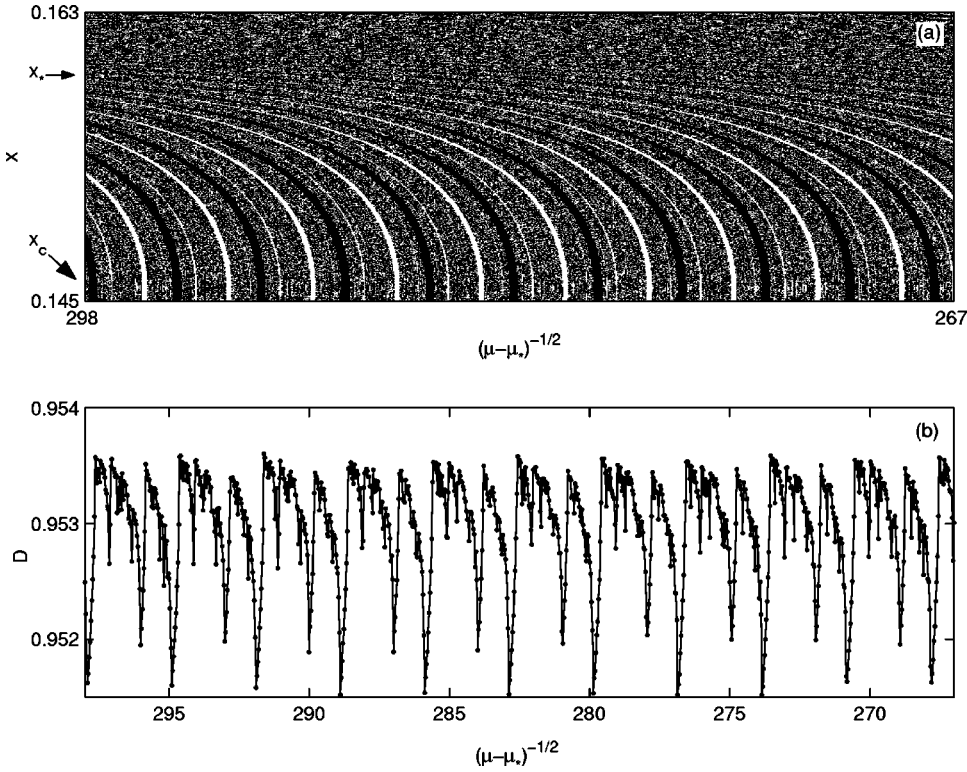
FIG. 4. (a) Detail of Fig. 2(b), with the horizontal axis changed from μ to $(\mu - \mu_*)^{-1/2}$ for $\mu > \mu_*$; The green stripes from Fig. 2(b) are colored black and the red stripes are colored white. The approximate position of the point x_* where the saddle-node bifurcation takes place is shown. x_c indicates the nearest critical point. (b) Detail of Fig. 3, displaying how the box dimension D of the fractal basin boundary varies with $(\mu - \mu_*)^{-1/2}$. The horizontal axes of (a) and (b) are identical.

small decrease in $\epsilon^{D_0 - D}$. This is discussed in Ref. [1] which defines the uncertainty dimension, D_u, as follows. Say we randomly pick an initial condition x with uniform probability density in a state-space region S. Then we randomly pick another initial condition y in S, such that $|y - x| < \epsilon$. Let $p(\epsilon, S)$ be the probability that x and y are in different basins. [We can think of $p(\epsilon, S)$ as the probability that an error will be made in determining the basin of an initial condition if the initial condition has uncertainty of size ϵ.] The uncertainty dimension of the basin boundary D_u is defined as the limit of $\ln p(\epsilon, S)/\ln(\epsilon)$ as ϵ goes to zero [1]. Thus, the probability of error scales as $p(\epsilon, S) \sim \epsilon^{D_0 - D_u}$, where for fractal basin boundaries $D_0 - D_u < 1$. This indicates enhanced sensitivity to the small uncertainty in initial conditions. For example, if $D_0 - D_u = 0.2$, then a decrease of the initial condition uncertainty ϵ by a factor of 10 leads to only a relatively small decrease in the final-state uncertainty $p(\epsilon, S)$, since p decreases by a factor of about $10^{0.2} \approx 1.6$. Thus, in practical terms, it may be essentially impossible to significantly reduce the final-state uncertainty. In Ref. [1] it was conjectured that the box-counting dimension equals the uncertainty dimension for basin boundaries in typical dynamical systems. In Ref. [17] it is proved that the box-counting dimension, the uncertainty dimension, and the Hausdorff dimension are all equal for the basin boundaries of one- and two-dimensional systems that are uniformly hyperbolic on their basin boundary.

We now explain some aspects of the character of the dependence of D on μ (see Fig. 3). From Ref. [18] it follows that the box-counting dimension and the Hausdorff dimension coincide for all intervals of μ for which the map f_μ is hyperbolic on the basin boundary and that the dimension depends continuously on the parameter μ in these intervals.

For $\mu > \mu_*$, there are many parameter values for which the map has a saddle-node bifurcation of a periodic orbit on the fractal basin boundary. At such parameter values, which we refer to as saddle-node bifurcation parameter values, the dimension is expected to be discontinuous (as it is at the saddle-node bifurcation of the fixed point, $\mu = \mu_*$; see Fig. 3). In fact, there exist sequences of saddle-node bifurcation parameter values converging to μ_* [16]. Furthermore, for each parameter value $\mu > \mu_*$ for which the map undergoes a saddle-node bifurcation, there exists a sequence of saddle-node bifurcation parameter values converging to that parameter value. The basins of attraction of the periodic orbits created by saddle-node bifurcations of high period exist only for very small intervals of the parameter μ. We did not encounter them numerically by iterating initial conditions for a discrete set of values of the parameter μ, as we did for the basin of our fixed-point attractor.

C. Scaling of the fractal basin boundary

Just past μ_*, the remaining green and red basins display an alternating stripe structure [see Fig. 2(b)]. The red and green stripes are interlaced in a fractal structure. As we approach the bifurcation point, the interlacing becomes finer and finer scaled, with the scale approaching zero as μ approaches μ_*. Similar fine-scale structure is present in the neighborhood of all preiterates of x_*. If one changes the horizontal axis of Figs. 2(a) and 2(b) from μ to $(\mu - \mu_*)^{-1/2}$, then the complex alternating stripe structure appears asymptotically periodic [see Fig. 4(a)]. [Thus, with identical horizontal scale, the dimension plot in Fig. 4(b) appears asymptotically periodic, as well.] We now explain

why this is so. We restrict our discussion to a small neighborhood of x_*. Consider the second-order expansion of f_μ in the vicinity of x_* and μ_*:

$$\hat{f}_{\hat{\mu}}(\hat{x}) = \hat{\mu} + \hat{x} + a\hat{x}^2, \quad \text{where} \begin{cases} \hat{x} = x - x_*, \\ \hat{\mu} = \mu - \mu_*, \end{cases} \quad (3)$$

and $a \approx 89.4315$. The trajectories of $\hat{f}_{\hat{\mu}}$ in the neighborhood of $\hat{x} = 0$, for $\hat{\mu}$ close to zero, are good approximations to trajectories of f_μ in the neighborhood of $x = x_*$, for μ close to μ_*. Assume that we start with a certain initial condition for $\hat{f}_{\hat{\mu}}$, $\hat{x}_0 = \hat{x}_s$, and we ask the following question: What are all the positive values of the parameter $\hat{\mu}$ such that a trajectory passes through a fixed position $\hat{x}_f > 0$ at some iterate n? For any given x_f which is not on the fractal basin boundary, there exists a range of μ such that iterates of x_f under f_μ evolve to the same final attractor, for all values of μ in that range. In particular, once $a\hat{x}^2$ appreciably exceeds $\hat{\mu}$, the subsequent evolution is approximately independent of $\hat{\mu}$. Thus, we can choose $\hat{x}_f \gg \sqrt{\hat{\mu}/a}$, but still small enough so that it lies in the region of validity of the canonical form (3). There exists a range of such $\hat{x}_f$ values satisfying these requirements provided that $|\hat{\mu}|$ is small enough.

Since consecutive iterates of $\hat{f}_{\hat{\mu}}$ in the neighborhood of $\hat{x} = 0$ for $\hat{\mu}$ close to zero differ only slightly, we approximate the one-dimensional map

$$\hat{x}_{n+1} = \hat{f}_{\hat{\mu}}(\hat{x}_n) = \hat{\mu} + \hat{x}_n + a\hat{x}_n^2 \quad (4)$$

by the differential equation [9]

$$\frac{d\hat{x}}{dn} = \hat{\mu} + a\hat{x}^2, \quad (5)$$

where in Eq. (5) n is considered as a continuous, rather than a discrete, variable. Integrating Eq. (5) from $\hat{x}_s$ to $\hat{x}_f$ yields

$$n\sqrt{a\hat{\mu}} = \arctan\left(\sqrt{\frac{a}{\hat{\mu}}}\hat{x}_f\right) - \arctan\left(\sqrt{\frac{a}{\hat{\mu}}}\hat{x}_s\right). \quad (6)$$

Close to the saddle-node bifurcation (i.e., $0 < \hat{\mu} \ll 1$ and $\hat{x}_{s,f}$ close to zero), $\hat{f}_{\hat{\mu}}$ is a good approximation to f_μ. For $|\hat{x}_{s,f}|\sqrt{(a/\hat{\mu})} \gg 1$, Eq. (6) becomes

$$n\sqrt{a\hat{\mu}} \approx \pi. \quad (7)$$

The values of $\hat{\mu}_n^{-1/2}$ satisfying Eq. (7) increase with n in steps of $\sqrt{a}/\pi$. For our example we have $a \approx 89.4315$; thus, $\sqrt{a}/\pi \approx 3.010$. Counting many periods like those in Fig. 4 in the region of x_c, the closest critical point to x_* [see Fig. 4(a)], we find that the period of the stripe structure is 3.015, which is in good agreement with our theoretical value.

In order to investigate the structure of the fractal basin boundary in the vicinity of the saddle-node bifurcation (i.e., $\hat{x}_s$ close to $\hat{x}_* = 0$), we consider Eq. (6) in the case where we demand only $|\hat{x}_f|\sqrt{(a/\hat{\mu})} \gg 1$. Thus, Eq. (6) becomes

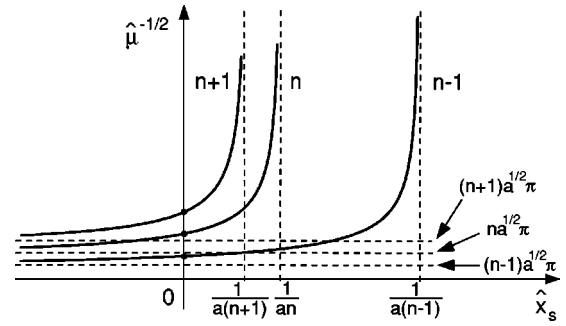FIG. 5. Qualitative graphs of the solution of Eq. (8), $\hat{\mu}_n^{-1/2}(\hat{x}_0)$, for three consecutive values of n. Note the horizontal asymptotes [$\hat{\mu}^{-1/2} = (n-1)a^{1/2}\pi$, $na^{1/2}\pi$, and $(n+1)a^{1/2}\pi$], the vertical asymptotes ($\hat{x}_s = [a(n-1)]^{-1}$, $(an)^{-1}$, and $[a(n+1)]^{-1}$), both shown as dashed lines, and the intersections of the solid curves with $\hat{x}_0 = 0$ which are marked with black dots.

$$n\sqrt{a\hat{\mu}} \approx \frac{\pi}{2} - \arctan\left(\sqrt{\frac{a}{\hat{\mu}}}\hat{x}_s\right). \quad (8)$$

Let $\hat{\mu}_n(\hat{x}_s)$ denote the solution of Eq. (8) for $\hat{\mu}$. Equation (8) implies the behavior of $\hat{\mu}_n^{-1/2}(\hat{x}_s)$ as function of $\hat{x}_s$ and n as sketched in Fig. 5. For a fixed n, $\hat{\mu}_n^{-1/2}$ has a horizontal asymptote at the value $n\sqrt{a}/\pi$ as $\hat{x}_s \to -\infty$ and a vertical asymptote to infinity at $\hat{x}_s = 1/(an)$. For $\hat{x}_s < 0$, we have an infinite number of values of the parameter $\hat{\mu}$, for which an orbit of $\hat{f}_{\hat{\mu}}$ starting at $\hat{x}_s$ passes through the same position $\hat{x}_f$, after some number of iterations. For $\hat{x}_s = 0$ (i.e., $x_s = x_*$), we also have an infinite number of $\hat{\mu}_n^{-1/2}(0)$, but with constant step $2\sqrt{a}/\pi$ rather than $\sqrt{a}/\pi$ (see the intersections marked with black dots in the Fig. 5). This is hard to verify from numerics, since $(\partial \hat{\mu}_n^{-1/2}/\partial \hat{x}_s)(0) = a^{3/2}(2n/\pi)^2$ increases with n^2, and the stripes become very tilted in the neighborhood of $\hat{x}_s = \hat{x}_* = 0$. [See Fig. 4(a), where the approximate positions of x_c and x_* on the vertical axis are indicated.] For $\hat{x}_s > 0$, $\hat{\mu}_n^{-1/2}$ has only a limited number of values with $n_{\max} < 1/(a\hat{x}_0)$.

D. Sweeping through an indeterminate saddle-node bifurcation

In order to understand the consequences of a saddle-node bifurcation on a fractal basin boundary for systems experiencing slow drift, we imagine the following experiment. We start with the dynamical system f_μ at parameter $\mu_s < \mu_*$, with x_0 on the attractor to be destroyed at $\mu = \mu_*$ by a saddle-node bifurcation (i.e., B_μ). Then, as we iterate, we slowly change μ by a small constant amount $\delta\mu$ per iterate, thus increasing μ from μ_s to $\mu_f > \mu_*$:

$$x_{n+1} = f_{\mu_n}(x_n),$$

$$\mu_n = \mu_s + n\delta\mu. \quad (9)$$

When $\mu \gtrsim \mu_f$ we stop sweeping the parameter μ, and by iterating further, we determine to which of the remaining attractors of f_{μ_f} the orbit goes. Numerically, we observe that,
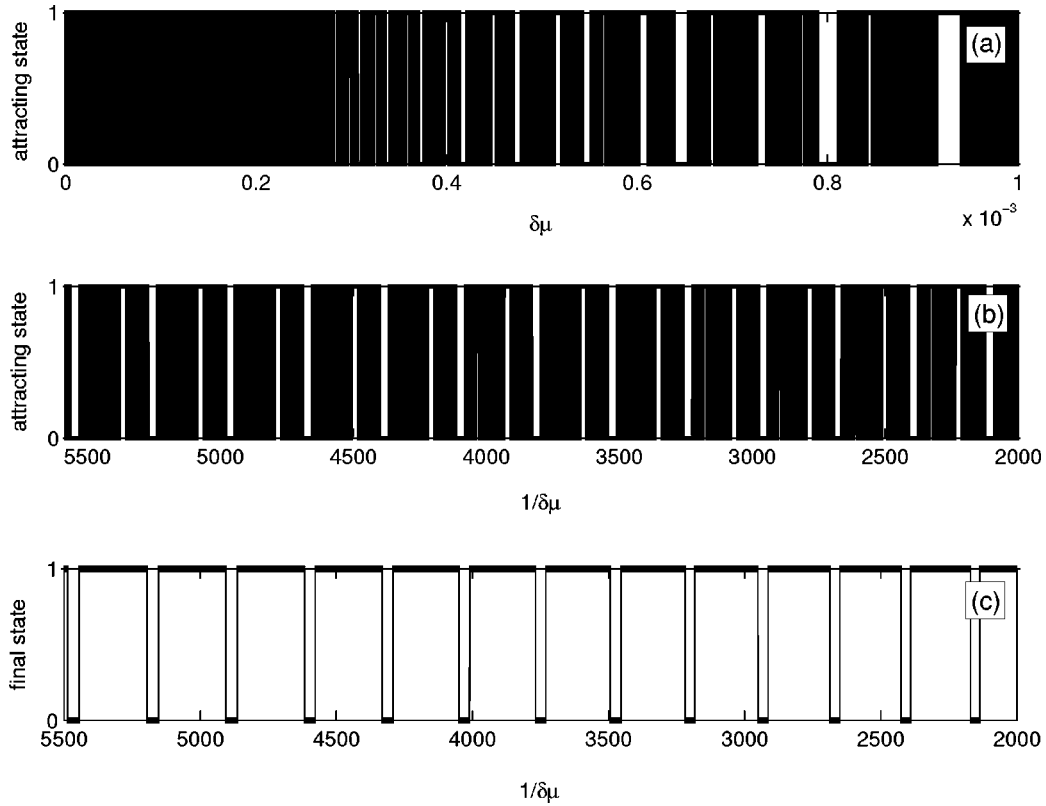
FIG. 6. (a) Final attracting state of swept orbits versus $\delta\mu$. We have chosen $\mu_s = \hat{\mu}_s + \mu_* = 0$ and $\mu_f = 4.5 \times 10^{-3}$. The attractor R_{μ_f} is represented by 1 and the attractor G_{μ_f} is represented by 0. (b) Detail of (a) with the horizontal scale changed from $\delta\mu$ to $1/\delta\mu$. The structure of white and black bands becomes asymptotically periodic. (c) Final state of orbits for the system $\hat{f}_{\hat{\mu}}$ versus $1/\delta\mu$. The final state of an orbit is defined to be 0 if there exists n such that $100 < \hat{x}_n < 250$ and is defined to be 1, otherwise. We have chosen $\hat{\mu}_s = -\mu_*$, so that (b),(c) have the same asymptotic periodicity.

if $(\mu_f - \mu_*)$ is not too small, then by the time μ_f is reached, the orbit is close to the attractor of f_{μ_f} to which it goes. [From our subsequent analysis, "not too small $|\mu_{s,f} - \mu_*|$" translates into choices of $\delta\mu$ that satisfy $(\delta\mu)^{2/3} \ll |\mu_{s,f} - \mu_*|$.] We repeat this for different values of $\delta\mu$ and we graph the final attractor position for the orbit versus $\delta\mu$ [see Fig. 6(a)]. For convenience in the graphical representation of Figs. 6(a) and 6(b), we have represented the attractor of the green region $G[\mu]$, denoted G_{μ_f}, as a 0, and the attractor of the red region $R[\mu]$, denoted R_{μ_f}, as a 1. In Fig. 6(a) we use 25 000 points having vertical coordinate of either 0 or 1, which we connect with straight lines. In an interval of $\delta\mu$ for which the system reaches the same final attractor (either 0 or 1), the lines connecting the points are horizontal. Such intervals appear as white bands in Fig. 6 if they are wider than the width of the plotted lines connecting 0's and 1's. For example, in Fig. 6(a), the white band centered at $\delta\mu = 0.8 \times 10^{-3}$ has at the bottom a thick horizontal line, which indicates that for the whole of that interval, the orbit reaches the attractor G_{μ_f} which we represented by 0. Adjacent intervals of width less than the plotted lines appear as black bands. Within such black bands, an uncertainty in $\delta\mu$ of size equal to the width of the plotted line makes the attractor that the orbit goes to indeterminate. Figure 6(a) shows that the

widths of the white bands decrease as $\delta\mu$ decreases, such that, for small $\delta\mu$, we see only black.

If $(\mu_f - \mu_*)$ is large enough [i.e., $(\delta\mu)^{2/3} \ll |\mu_f - \mu_*|$], numerics and our subsequent analysis show that Fig. 6 is independent of μ_f. This fact can be understood as follows. Once $\mu = \mu_f$, the orbit typically lands in the green or the red basin of attraction and goes to the corresponding attractor. Due to sweeping, it is possible for the orbit to switch from being in one basin of attraction of the *time-independent* map f_μ to the other, since the basin boundary between $G[\mu]$ and $R[\mu]$ changes with μ. However, the sweeping of μ is slow (i.e., $\delta\mu$ is small), and once $(\mu - \mu_*)$ is large enough, the orbit is far enough from the fractal basin boundary, and the fractal basin boundary changes too little to switch the orbit between $G[\mu]$ and $R[\mu]$.

We also find numerically that Figs. 6(a) and 6(b) are independent of the initial condition x_0, provided that it is in the blue basin $B[\mu_s]$, sufficiently far from the fractal basin boundary, and that $|\mu_s - \mu_*|$ is not too small [i.e., $(\delta\mu)^{2/3} \ll |\mu_s - \mu_*|$].

If one changes the horizontal scale of Fig. 6(a) from $\delta\mu$ to $1/\delta\mu$ [see Fig. 6(b)], the complex band structure appears asymptotically periodic. Furthermore, we find that the period in $(1/\delta\mu)$ of the structure in Fig. 6(b) asymptotically approaches $-1/(\mu_s - \mu_*)$ as $\delta\mu$ becomes small.

In order to explain this result, we again consider the map $\hat{f}_{\hat{\mu}}$, the local approximation of f_μ in the region of the saddle-node bifurcation. Equations (9) can be approximated by

$$\hat{x}_{n+1} = \hat{f}_{\hat{\mu}_n}(\hat{x}_n) = \hat{\mu}_n + \hat{x}_n + a\hat{x}_n^2,$$

$$\hat{\mu}_n = \hat{\mu}_s + n\,\delta\mu. \qquad (10)$$

We perform the following numerical experiment. We consider orbits of our approximate two-dimensional map given by Eq. (10) starting at $\hat{x}_s = -\sqrt{-\hat{\mu}_s/a}$. We define a final-state function of an orbit swept with parameter $\delta\mu$ in the following way. It is 0 if the orbit has at least one iterate in a specified fixed interval far from the saddle-node bifurcation and is 1 otherwise. In particular, we take the final state of a swept orbit to be 0 if there exists n such that $100 < \hat{x}_n < 250$ and to be 1 otherwise. Figure 6(c) graphs the corresponding numerical results. Similar to Fig. 6(b), we observe periodic behavior in $1/\delta\mu$ with period $-1/\hat{\mu}_s$. In contrast to Fig. 6(b) where the white band structure seems fractal, the structure within each period in Fig. 6(c) consists of only one interval where the final state is 0 and one interval where the final state is 1. This is because $100 < \hat{x} < 250$ is a single interval, while the green basin [denoted 0 in Fig. 6(b)] has an infinite number of disjoint intervals and a fractal boundary (see Fig. 2).

With the similarity between Figs. 6(b) and 6(c) as a guide, we are now in a position to give a theoretical analysis explaining the observed periodicity in $1/\delta\mu$. In particular, we now know that this can be explained using the canonical map (10) and that the periodicity result is thus universal [i.e., independent of the details of our particular example, Eq. (1)]. For slow sweeping (i.e., $\delta\mu$ small), consecutive iterates of Eqs. (10) in the vicinity of $\hat{x} = 0$ and $\hat{\mu} = 0$ differ only slightly, and we further approximate the system by the following Ricatti differential equation:

$$\frac{d\hat{x}}{dn} = \hat{\mu}_s + n\,\delta\mu + a\hat{x}^2. \qquad (11)$$

The solution of Eq. (11) can be expressed in terms of the Airy functions Ai and Bi and their derivatives, denoted by Ai′ and Bi′:

$$\hat{x}(n) = \frac{\eta\,\mathrm{Ai}'(\xi) + \mathrm{Bi}'(\xi)}{\eta\,\mathrm{Ai}(\xi) + \mathrm{Bi}(\xi)}\left(\frac{\delta\mu}{a^2}\right)^{1/3}, \qquad (12)$$

where

$$\xi(n) = -a^{1/3}\frac{\hat{\mu}_s + n\,\delta\mu}{\delta\mu^{2/3}} \qquad (13)$$

and η is a constant to be determined from the initial condition. We are only interested in the case of slow sweeping, $\delta\mu \ll 1$, and $\hat{x}(0) \equiv \hat{x}_s = -\sqrt{-\hat{\mu}_s/a}$ (which is the stable fixed point of $\hat{f}_{\hat{\mu}}$ destroyed by the saddle-node bifurcation at $\hat{\mu} = 0$). In particular, we will consider the case where $\hat{\mu}_s < 0$ and $|\hat{\mu}_s| \gg \delta\mu^{2/3}$ [i.e., $|\xi(0)| \gg 1$]. Using $\hat{x}(0) = -\sqrt{-\hat{\mu}_s/a}$

to solve for η yields $\eta \sim \mathcal{O}[\xi(0)e^{2\xi(0)}] \gg 1$. For positive large values of $\xi(n)$ (i.e., for n small enough), using the corresponding asymptotic expansions of the Airy functions [19], the lowest order in $\delta\mu$ approximation to Eq. (12) is

$$\hat{x}(n) \approx -\sqrt{-\frac{\hat{\mu}_s + n\,\delta\mu}{a}}, \qquad (14)$$

with the correction term of higher order in $\delta\mu$ being negative. Thus, for n sufficiently smaller than $-\hat{\mu}_s/\delta\mu$, the swept orbit lags closely behind the fixed point for $\hat{f}_{\hat{\mu}}$ with $\hat{\mu}$ constant. For $\xi \lesssim 0$, we use the fact that η is large to approximate Eq. (12) as

$$\hat{x}(n) \approx \frac{\mathrm{Ai}'(\xi)}{\mathrm{Ai}(\xi)}\left(\frac{\delta\mu}{a^2}\right)^{1/3}. \qquad (15)$$

Note that

$$\hat{x}(-\hat{\mu}_s/\delta\mu) \approx \frac{\mathrm{Ai}'(0)}{\mathrm{Ai}(0)}\left(\frac{\delta\mu}{a^2}\right)^{1/3} = (-0.7290\ldots)\left(\frac{\delta\mu}{a^2}\right)^{1/3} \qquad (16)$$

gives the lag of the swept orbit relative to the fixed-point attractor evaluated at the saddle-node bifurcation. Equation (15) does not apply for $n > n_{max}$, where n_{max} is the value of n for which $\xi(n_{max}) = \tilde{\xi}$, the largest root of $\mathrm{Ai}(\tilde{\xi}) = 0$ (i.e., $\tilde{\xi} = -2.3381\ldots$). At $n = n_{max}$, the normal-form approximation predicts that the orbit diverges to $+\infty$. Thus, for n near n_{max}, the normal-form approximation of the dynamical system ceases to be valid. Note, however, that Eq. (15) can be valid even for $\xi(n)$ close to $\xi(n_{max})$. This is possible because $\delta\mu$ is small. In particular, we can consider times up to the time n' where n' is determined by $\xi' \equiv \xi(n') = \tilde{\xi} + \delta\xi$ ($\delta\xi > 0$ is small) provided $|\hat{x}(n')| \ll 1$ so that the normal form applies. That is, we require $[\mathrm{Ai}'(\xi')/\mathrm{Ai}(\xi')](\delta\mu/a^2)^{1/3} \ll 1$, which can be satisfied even if $[\mathrm{Ai}'(\xi')/\mathrm{Ai}(\xi')]$ is large. Furthermore, we will take the small quantity $\delta\xi$ to be not too small [i.e., $\delta\xi/(a\,\delta\mu)^{1/3} \gg 1$], so that $(n_{max} - n') \gg 1$. We then consider Eq. (15) in the range $-(\hat{\mu}_s/\delta\mu) \leq n < n'$, where the normal form is still valid.

We use Eq. (15) for answering the following question: What are all the values of the parameter $\delta\mu$ ($\delta\mu$ small) for which an orbit passes exactly through the same position $\hat{x}_f > 0$ at some iterate n_f? All such orbits would further evolve to the same final attractor, independent of $\delta\mu$, provided $a\hat{x}_f^2 \gg \hat{\mu}_s + n_f\delta\mu$—i.e., $\hat{x}_f$ is large enough that $\hat{\mu}_f = \hat{\mu}_s + n_f\,\delta\mu$ does not much influence the orbit after $\hat{x}$ reaches $\hat{x}_f$. [Denote $\xi(n_f)$ as $\xi(n_f) \equiv \xi_f$.] Using Eq. (15) we can estimate when this occurs, $a\hat{x}_f^2 = [\mathrm{Ai}'(\xi_f)/\mathrm{Ai}(\xi_f)]^2(\delta\mu^2/a)^{1/3} \gg (\hat{\mu}_s + n_f\,\delta\mu)$ or $[\mathrm{Ai}'(\xi_f)/\mathrm{Ai}(\xi_f)]^2 \gg \xi_f$. This inequality is satisfied when ξ_f gets near $\tilde{\xi}$, which is the largest zero of Ai (i.e., $\xi_f = \tilde{\xi} + \delta\xi$, where $\delta\xi$ is a small positive quantity). We now rewrite Eq. (15) in the following way:

FIG. 8. Qualitative graphs of $\hat{f}_{\hat{\mu}}(\hat{x})$ in the vicinity of the saddle-node bifurcation at different values of the parameter $\hat{\mu}$. The black dots indicate the stable fixed points of $\hat{f}_{\hat{\mu}}$ for different values of $\hat{\mu}$.
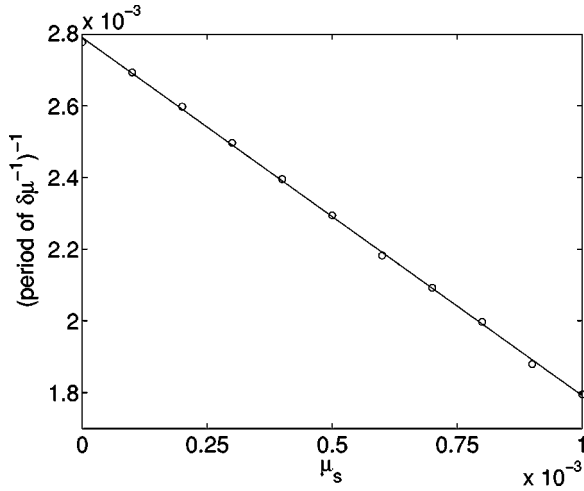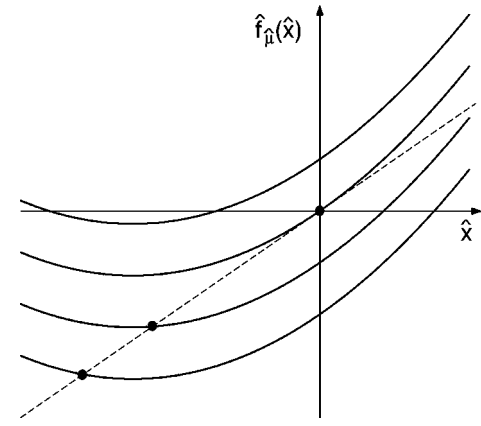
FIG. 7. Numerical results for the inverse of the limit period in $1/\delta\mu$ versus μ_s. The fit line is $[\Delta(1/\delta\mu)]^{-1} = -0.9986\mu_s + 0.0028$ and indicates good agreement with the theoretical explanation presented in text.

$$\frac{1}{\delta\mu} = - \frac{n_f}{\hat{\mu}_s - \left[\frac{(\delta\mu)^2}{a}\right]^{1/3} K\left[\left(\frac{a^2}{\delta\mu}\right)^{1/3} \hat{x}_f\right]}, \quad (17)$$

representing a transcedental equation in $\delta\mu$ where $\hat{\mu}_s$ and $\hat{x}_f$ are fixed, n_f is a large positive integer [i.e., $n_f - 1$ is the integer part of $(\hat{\mu}_f - \hat{\mu}_s)/\delta\mu$], and $K(\zeta)$ is the inverse function of $\mathrm{Ai}'(\xi)/\mathrm{Ai}(\xi)$ in the neighborhood of $\zeta = (a^2/\delta\mu)^{1/3}\hat{x}_f \gg 1$. Thus $|K[(a^2/\delta\mu)^{1/3}\hat{x}_f]| \lesssim |K(\infty)| = |\bar{\xi}|$. The difference $[1/\delta\mu(x_f, n_f + 1) - 1/\delta\mu(x_f, n_f)]$, where $\delta\mu(x_f, n_f)$ is the solution of Eq. (17), yields the limit period of the attracting state versus $1/\delta\mu$ graph (see Fig. 6). We denote this limit period by $\Delta(1/\delta\mu)$. For small $\delta\mu$, the term involving $K[(a^2/\delta\mu)^{1/3}\hat{x}_f]$ in Eq. (17) can be neglected, and we get $\Delta(1/\delta\mu) = -\hat{\mu}_s^{-1} = (-\mu_s + \mu_*)^{-1}$. Figure 7 graphs numerical results of $[\Delta(1/\delta\mu)]^{-1}$ versus μ_s for our map example given by Eq. (9). The fit line is $[\Delta(1/\delta\mu)]^{-1} = -0.9986\mu_s + 0.0028$, which agrees well with the prediction of the above analysis and our numerical value for μ at the bifurcation, $\mu_* \approx 0.00279$.

An alternate point of view on this scaling property is as follows. For $\hat{\mu} < 0$ (i.e., $\mu < \mu_*$) and slow sweeping (i.e., $\delta\mu$ small), the orbit closely follows the stable fixed-point attrac-

tor of $\hat{f}_{\hat{\mu}}$, until $\hat{\mu} \geq 0$, and the saddle-node bifurcation takes place. However, due to the discreteness of n, the first non-negative value of $\hat{\mu}$ depends on $\hat{\mu}_s$ and $\delta\mu$ (see Fig. 8). Now consider two values of $\delta\mu$: one $\delta\mu_m$ satisfying $\hat{\mu}_s + m\delta\mu_m = 0$ and another $\delta\mu_{m+1}$ satisfying $\hat{\mu}_s + (m+1)\delta\mu_{m+1} = 0$. Because $\delta\mu_m$ and $\delta\mu_{m+1}$ are very close (for large m) *and* both lead $\hat{\mu}(n)$ to pass through $\hat{\mu} = \hat{\mu}_* = 0$ (one at time $n = m$ and the other at time $n = m + 1$), it is reasonable to assume that their orbits for $\hat{\mu}_s/\delta\mu < n < n'$ are similar (except for a time shift $n \to n + 1$); i.e., they go to the same attractor. Thus, the period of $1/\delta\mu$ is approximately $\Delta(1/\delta\mu) = 1/\delta\mu_{m+1} - 1/\delta\mu_m = -\hat{\mu}_s^{-1}$.

We now consider the intervals of $1/\delta\mu$ between the centers of consecutive wide white bands in Fig. 6(b). Figure 9 graphs the calculated fractal dimension D' of the boundary between white bands in these consecutive intervals versus their center value of $1/\delta\mu$. From Fig. 9, we see that as $1/\delta\mu$ increases, the graph of the fractal dimension D' does not converge to a definite value, but displays further structure. Nevertheless, numerics show that as $1/\delta\mu$ becomes large (i.e., in the range of 6.5×10^5), D' varies around the value 0.952. This is consistent with the numerics presented in Fig. 4(b) which graphs the dimension of the fractal basin boundary for the time-independent map f_μ at fixed values of the parameter μ where $\mu > \mu_*$. Thus, for large $1/\delta\mu$, D' provides an estimate of the dimension of the fractal basin boundary in the absence of sweeping at $\mu > \mu_*$.
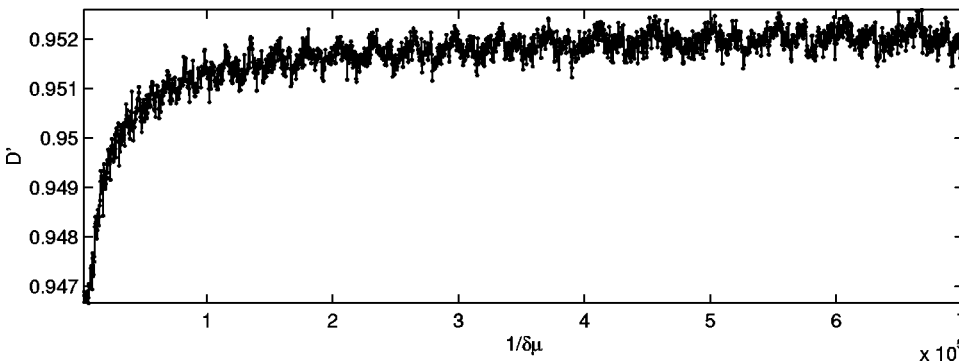

FIG. 9. The calculated fractal dimension D' of the structure in the intervals between the centers of consecutive wide white bands in Fig. 6(b) versus their center value of $1/\delta\mu$.
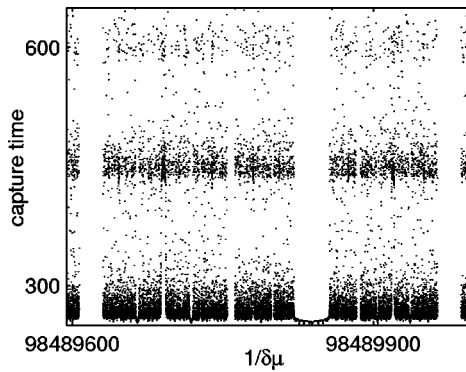
FIG. 10. Capture time by the fixed-point attractor G_{μ_f} versus $1/\delta\mu$. We have chosen $\mu_s = 0$. The range of $1/\delta\mu$ is approximately one period of the graph in Fig. 6(b). No points are plotted for values of $\delta\mu$ for which the orbit reaches the fixed-point attractor R_{μ_f}.

We now discuss a possible experimental application of our analysis. The conceptually most straightforward method of measuring a fractal basin boundary would be to repeat many experiments each with precisely chosen initial conditions. By determining the final attractor corresponding to each initial condition, basins of attraction could conceivably be mapped out [3]. However, it is commonly the case that accurate control of initial conditions is not feasible for experiments. Thus, the application of this direct method is limited, and as a consequence, fractal basin boundaries have received little experimental study, in spite of their fundamental importance. If a saddle-node bifurcation occurs on the fractal basin boundary, an experiment can be arranged to take advantage of this. In this case, the purpose of the experiment would be to measure the dimension D' as an estimate of the fractal dimension of the basin boundary D. The measurements would determine the final attractor of orbits starting at the attractor to be destroyed by the saddle-node bifurcation and swept through the saddle-node bifurcation at different velocities (i.e., the experimental data corresponding to the numerics in Fig. 6). This does not require precise control of the initial conditions of the orbits. It is sufficient for the initial condition to be in the basin of the attractor to be destroyed by the saddle-node bifurcation; after enough time, the orbit will be as close to the attractor as the noise level allows. Then, the orbit may be swept through the saddle-node bifurcation. The final states of the orbits are attractors; in their final states, orbits are robust to noise and to measurement perturbations. The only parameters which require rigorous control are the sweeping velocity (i.e., $\delta\mu$) and the initial value of the parameter to be swept (i.e., μ_s); precise knowledge of the parameter value where the saddle-node bifurcation takes place (i.e., μ_*) is not needed. [It is also required that the noise level be sufficiently low (see Sec. II F).]

E. Capture time

A question of interest is how much time it takes for a swept orbit to reach the final attracting state. Namely, we ask how many iterations with $\mu > \mu_*$ are needed for the orbit to reach a neighborhood of the attractor having the green basin. Due to slow sweeping, the location of the attractor changes

slightly on every iterate. If x_μ is a fixed-point attractor of f_μ (with μ constant), then a small change $\delta\mu$ in the parameter μ yields a change in the position of the fixed-point attractor:

$$(x_{\mu+\delta\mu} - x_\mu) \equiv \delta x = \delta\mu \frac{(\partial f/\partial\mu)(x_\mu; \mu)}{1 - (\partial f_\mu/\partial x)(x_\mu)}.$$

We consider the swept orbit to have reached its final attractor if consecutive iterates differ by about δx (which is proportional to $\delta\mu$). For numerical purposes, we consider that the orbit has reached its final state if $|x_{n+1} - x_n| < 10\delta\mu$. In our numerical experiments, this condition is satisfied by every orbit before μ reaches its final value μ_f. We refer to the number of iterations with $\mu > \mu_*$ needed to reach the final state as the *capture time* of the corresponding orbit. Figure 10 plots the capture time by the attractor G_{μ_f} (having the green basin in Fig. 2) versus $1/\delta\mu$ for a range corresponding to one period of the structure in Fig. 6(b). No points are plotted for values of $\delta\mu$ for which the orbit reaches the attractor R_{μ_f}. The capture time graph has fractal features, since for many values of $\delta\mu$ the orbit gets close to the fractal boundary between $R[\mu]$ and $G[\mu]$. Using the fact that the final destination of the orbit versus $1/\delta\mu$ is asymptotically periodic [see Fig. 6(b)], we can provide a further description of the capture time graph. We consider the series of the largest intervals of $1/\delta\mu$ for which the orbit reaches the attractor G_{μ_f} [see Fig. 6(b); we refer to the wide white band around $1/\delta\mu = 2400$ and the similar ones which are (asymptotically) separated by an integer number of periods]. Orbits swept with $\delta\mu$ at the centers of these intervals spend only a small number of iterations close to the common fractal boundary of $R[\mu]$ and $G[\mu]$. Thus, the capture time of such similar orbits does not depend on the structure of the fractal basin boundary. We use Eq. (15) as an approximate description of these orbits. A swept orbit reaches its final attracting state as $\hat{x}(n)$ becomes large. Then, the orbit is rapidly trapped in the neighborhood of one of the swept attractors of f_μ. Thus, we equate the argument of the Airy function in the denominator to its first root [see Eq. (15)], solve for n, and subtract
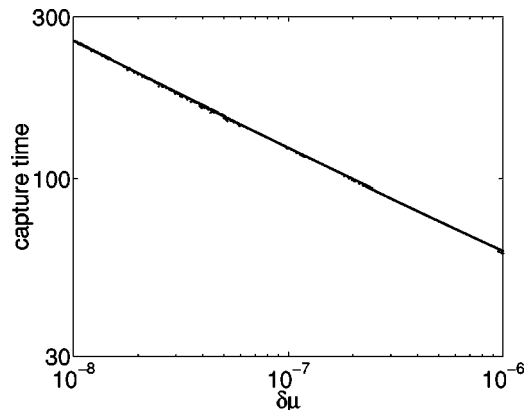

FIG. 11. Capture time by the middle fixed-point attractor of f_μ versus $\delta\mu$ ($\mu_s = 0$). The best fitting line (not shown) has slope -0.31, in agreement with the theory.

$-\hat{\mu}_s/\delta\mu$ (the time for $\hat{\mu}$ to reach the bifurcation value). This yields the following approximate formula for the capture time:

$$n_C \approx |\tilde{\xi}|(a\,\delta\mu)^{-1/3}, \quad (18)$$

where $\tilde{\xi} = -2.3381\ldots$ is the largest root of the Airy function Ai. Thus, we predict that for small $\delta\mu$, a log-log plot of the capture time of the selected orbits versus $\delta\mu$ is a straight line with slope $-1/3$. Figure 11 shows the corresponding numerical results. The best fitting line (not shown) has slope -0.31, in agreement with our prediction [20].

F. Sweeping through an indeterminate saddle-node bifurcation in the presence of noise

We now consider the addition of noise. Thus, we change our swept dynamical system to

$$x_{n+1} = f_{\mu_n}(x_n) + A\,\epsilon_n,$$

$$\mu_n = \mu_s + n\,\delta\mu, \quad (19)$$

where ϵ_n is random with uniform probability density in the interval $[-1,1]$ and A is a parameter which we call the noise amplitude. See Fig. 6(a) which shows the numerical results of the final destination of the orbits versus $\delta\mu$ in the case $A=0$. The graph exhibits fractal features of structure at arbitrarily small scales. The addition of small noise is expected to alter this structure, switching the final destination of orbits. In this case, it is appropriate to study the probability of orbits reaching one of the final destinations. For every A, we compute the final attractor of a large number of orbits having identical initial condition and parameters, but with different realizations of the noise. We estimate the probability that an orbit reaches a certain attractor by the fraction of such orbits that have reached the specified attractor in our numerical simulation. Figure 12 graphs the probability that an orbit reaches the attractor G_{μ_f} versus the noise amplitude A. We present five graphs corresponding to five different values of $\delta\mu$ equally spaced in a range of 10^{-7} centered at 10^{-5} (i.e., $\delta\mu=10^{-5}$, $10^{-5}\pm2.5\times10^{-8}$, and $10^{-5}\pm5\times10^{-8}$). We notice that the probability graphs have different shapes, but a common horizontal asymptote in the limit of large noise. The value of the horizontal asymptote, approximately equal to 0.5, is related to the relative measure of the corresponding basin.
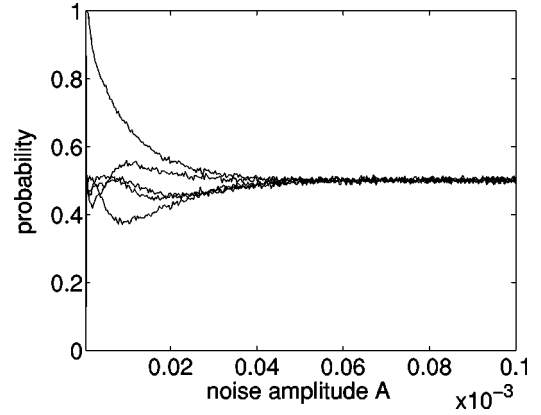

FIG. 12. Probability that one orbit reaches the middle fixed-point attractor of f_μ versus the noise amplitude A, for five different values of $\delta\mu$ (10^{-5}, $10^{-5}\pm2.5\times10^{-8}$ and $10^{-5}\pm5\times10^{-8}$). We have chosen $\mu_s=0$.

As in the previous subsection, we take advantage of the asymptotically periodic structure of the noiseless final destination graph versus $1/\delta\mu$ [see Fig. 6(b)]. We consider centers of the largest intervals of $1/\delta\mu$ for which an orbit reaches the middle attractor in the absence of noise. We chose five such values of $\delta\mu$, spread over two decades, where the ratio of consecutive values is approximately 3. Figure 13(a) graphs the probability that an orbit reaches the middle fixed-point attractor versus the noise amplitude A for the five selected values of $\delta\mu$. We notice that all the curves have qualitatively similar shape. For a range from zero to small A, the probability is 1, and as A increases, the probability decreases to a horizontal asymptote. The rightmost curve in the family corresponds to the largest value of $\delta\mu$ ($\delta\mu\approx3.445\,974\times10^{-5}$), and the leftmost curve corresponds to the smallest value of $\delta\mu$ ($\delta\mu\approx4.243\,522\times10^{-7}$). Figure 13(b) shows the same family of curves as in Fig. 13(a), but with the horizontal scale changed from A to $A/(\delta\mu)^{5/6}$. All data collapse to a single curve, indicating that the probability that a swept orbit reaches the attractor G_{μ_f} depends only on the reduced variable $A/(\delta\mu)^{5/6}$. Later, we provide a theoretical argument for this scaling.

In order to gain some understanding of this result, we follow the idea of Sec. II D and use the canonical form $\hat{f}_{\hat{\mu}}$ to propose a simplified setup of our problem. We modify Eqs. (10) by the addition of a noise term $A\epsilon_n$ in the right-hand side of the first equation of Eqs. (10). We are interested in the probability that a swept orbit has at least one iterate $\hat{x}_n$ in a
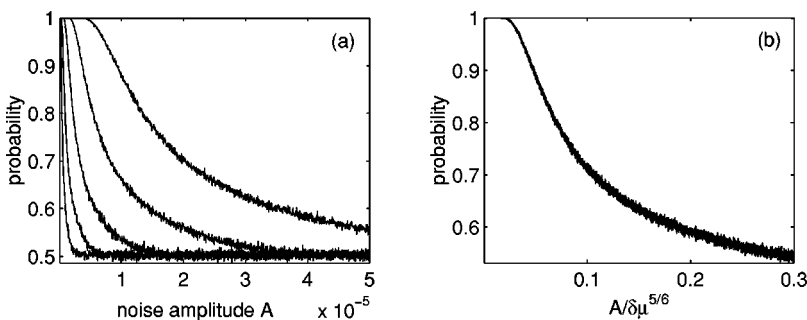

FIG. 13. Probability that an orbit reaches the middle fixed-point attractor of f_μ, for five selected values of $\delta\mu$ spread over two decades: (a) versus the noise amplitude A and (b) versus $A/(\delta\mu)^{5/6}$. We have chosen $\mu_s=0$. From right to left, the $\delta\mu$ values corresponding to the curves are approximately $3.445\,974\times10^{-5}$, $1.147\,767\times10^{-5}$, $3.820\,744\times10^{-6}$, $1.273\,160\times10^{-6}$, and $4.243\,522\times10^{-7}$.
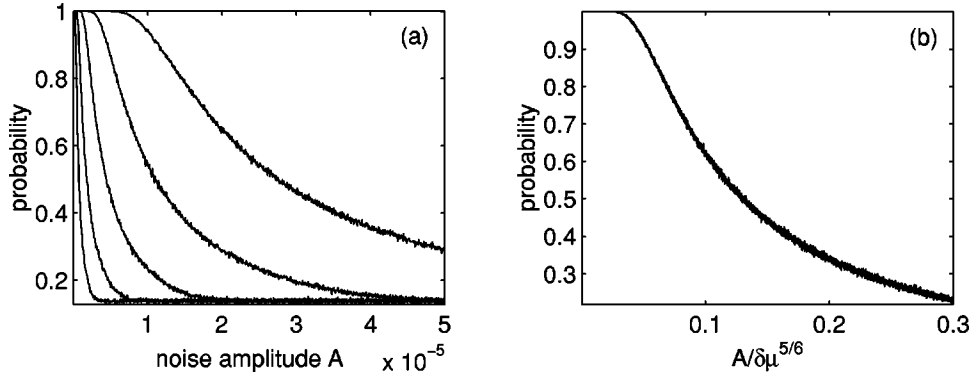
FIG. 14. Probability that an orbit of $\hat{f}_{\hat{\mu}}$ reaches a fixed interval far from the saddle-node bifurcation (i.e., [100, 250]), for five values of $\delta\mu$ spread over two decades: (a) versus the noise amplitude A, and (b) versus $A/(\delta\mu)^{5/6}$. We have chosen $\mu_s = 0$. From right to left, the $\delta\mu$ values corresponding to the curves are approximately $3.451\,540\times10^{-5}$, $1.149\,162\times10^{-5}$, $3.829\,769\times10^{-6}$, $1.276\,061\times10^{-6}$, and $4.253\,018\times10^{-7}$.

specified fixed interval far from the vicinity of the saddle-node bifurcation. More precisely, we analyze how this probability changes versus A and $\delta\mu$. Depending on the choice of interval and the choice of $\delta\mu$, the graph of the probability versus A (not shown) has various shapes. For numerical purposes, we choose our fixed interval to be the same as that of Sec. II D, $100 < \hat{x} < 250$. We then select values of $\delta\mu$ for which a noiseless swept orbit, starting at $\hat{x}_s = -\sqrt{-\hat{\mu}_s/a}$, reaches exactly the center of our fixed interval. The inverse of these values of $\delta\mu$ are centers of intervals where the final state of the swept orbits is 0 [see Fig. 6(c)]. We consider five such values of $\delta\mu$, where the ratio of consecutive values is approximately 3. Figure 14(a) shows the probability that a swept orbit has an iterate in our fixed interval versus the noise amplitude for the selected values of $\delta\mu$. Figure 14(a) shares the qualitative characteristics of Fig. 13(a), with the only noticeable difference that the value of the horizontal asymptote is now approximately 0.1. Figure 14(b) shows the same family of curves as in Fig. 14(a), where the horizontal scale has been changed from A to $A/(\delta\mu)^{5/6}$. As for Fig. 12(b), this achieves good collapse of the family of curves.

We now present a theoretical argument for why the probability of reaching an attractor depends on $\delta\mu$ and A only through the scaled variable $A/(\delta\mu)^{5/6}$ when $\delta\mu$ and A are small. From our results in Fig. 14, we know that the scaling we wish to demonstrate should be obtainable by use of the canonical form $\hat{f}_{\hat{\mu}}$. Accordingly, we again use the differential equation approximation (11), but with a noise term added,

$$\frac{d\hat{x}}{dn} = n\,\delta\mu + a\hat{x}^2 + A\,\hat{\epsilon}(n), \qquad (20)$$

where $\hat{\epsilon}(n)$ is white noise,

$$\langle\hat{\epsilon}(n)\rangle = 0, \quad \langle\hat{\epsilon}(n+n')\hat{\epsilon}(n)\rangle = \delta(n'),$$

and we have redefined the origin of the time variable n so that the parameter $\hat{\mu}$ sweeps through zero at $n=0$ (i.e., we replaced n by $n - |\hat{\mu}_s|/\delta\mu$). Because we are only concerned

with scaling and not with an exact solution of Eq. (20), a fairly crude analysis will be sufficient.

First we consider a solution of Eq. (20) with the noise term omitted and the initial condition [see Eq. (16)]

$$\hat{x}(0) = (-0.7290\ldots)(\delta\mu/a^2)^{1/3}.$$

We define a characteristic point of the orbit, $\hat{x}_{\mathrm{nl}}(n_{\mathrm{nl}})$, where $a\hat{x}_{\mathrm{nl}}^2 \approx n_{\mathrm{nl}}\,\delta\mu$. For $n < n_{\mathrm{nl}}$, $n\,\delta\mu \lesssim d\hat{x}/dn < 2n\,\delta\mu$, and we can approximate the noiseless orbit as

$$\hat{x}(n) \approx \hat{x}(0) + \alpha(n)(n^2\,\delta\mu), \qquad (21)$$

where $\alpha(n)$ is a slowly varying function of n of order 1 [$1/2 \leq \alpha(n) < 1$ for $n < n_{\mathrm{nl}}$]. Setting $a\hat{x}^2 \approx n\,\delta\mu$, we find that n_{nl} is given by

$$n_{\mathrm{nl}} \sim (a\,\delta\mu)^{-1/3}, \qquad (22)$$

corresponding to [cf. Eq. (21)]

$$\hat{x}_{\mathrm{nl}} \sim (\delta\mu/a^2)^{1/3}.$$

For $n > n_{\mathrm{nl}}$ [i.e., $\hat{x}(n) > \hat{x}_{\mathrm{nl}}$], Eq. (20) can be approximated as $d\hat{x}/dn \approx a\hat{x}^2$. Starting at $\hat{x}(n) \sim \hat{x}_{\mathrm{nl}}$, integration of this equation leads to explosive growth of $\hat{x}$ to infinity in a time of order $(a\,\delta\mu)^{-1/3}$, which is of the same order as n_{nl}. Thus, the relevant time scale is $(a\,\delta\mu)^{-1/3}$ [this agrees with Eq. (18) in Sec. II E].

Now consider the action of noise. For $n < n_{\mathrm{nl}}$, we neglect the nonlinear term $a\hat{x}^2$, so that Eq. (20) becomes $d\hat{x}/dn = n\,\delta\mu + A\hat{\epsilon}(n)$. The solution of this equation is the linear superposition of the solutions of $d\hat{x}_a/dn = n\,\delta\mu$ and $d\hat{x}_b/dn = A\hat{\epsilon}(n)$, or $\hat{x}(n) = \hat{x}_a(n) + \hat{x}_b(n)$; $\hat{x}_a(n)$ is given by $\hat{x}_a(n) = \hat{x}(0) + n^2\delta\mu/2$, and $\hat{x}_b(n)$ is a random walk. Thus, for $n < n_{\mathrm{nl}}$, there is diffusive spreading of the probability density of $\hat{x}$:

$$\Delta_{\mathrm{diff}}(n) \equiv \sqrt{\langle\hat{x}_b^2(n)\rangle} \sim n^{1/2}A. \qquad (23)$$

This diffusive spreading can blur out the structure in Fig. 6. How large does the noise amplitude A have to be to do this? We can estimate A by noting that the periodic structure in
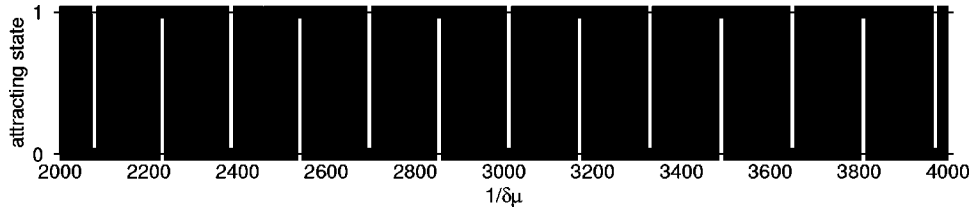
FIG. 15. Final attracting state of swept orbits of the Duffing oscillator versus $1/\delta\mu$. The structure of white and black bands becomes asymptotically periodic. We have chosen $\mu_s = 0.253$ and $\mu_f = 0.22$. The attractor in the potential well for $x > 0$ is represented as a 1, and the attractor in the potential well for $x < 0$ is represented as a 0.

Figs. 6(b) and 6(c) results from orbits that take different integer times to reach $\hat{x} \sim \hat{x}_{nl}$. Thus, for $n \approx n_{nl}$ we define a scale Δ_{nl} in $\hat{x}$ corresponding to the periodicity in $1/\delta\mu$ by [cf. Eq. (21)]

$$\hat{x}_{nl} \pm \Delta_{nl} \approx \hat{x}(0) + (n_{nl} \pm 1)^2 \ \delta\mu,$$

which yields

$$\Delta_{nl} \sim n_{nl} \ \delta\mu. \tag{24}$$

If by the time $n \approx n_{nl}$ the diffusive spread of the probability density of $\hat{x}$ becomes as large as Δ_{nl}, then the noise starts to wash out the periodic variations with $1/\delta\mu$. Setting $\Delta_{diff}(n_{nl})$ from Eq. (23) to be of the order of Δ_{nl} from Eq. (24), we obtain $n_{nl}^{1/2} A \sim n_{nl} \ \delta\mu$, which with Eq. (22) yields

$$A \sim (\delta\mu)^{5/6}. \tag{25}$$

Thus, we expect a collapse of the two-parameter $(A, \delta\mu)$ data in Fig. 14(a) by means of a rescaling of A by $\delta\mu$ raised to an exponent 5/6 [i.e., $A/(\delta\mu)^{5/6}$].

III. SCALING OF INDETERMINATE SADDLE-NODE BIFURCATIONS FOR A PERIODICALLY FORCED SECOND-ORDER ORDINARY DIFFERENTIAL EQUATION

In this section we demonstrate the scaling properties of sweeping through an indeterminate saddle-node bifurcation in the case of the periodically forced Duffing oscillator [12]:

$$\ddot{x} - 0.15\dot{x} - x + x^3 = \mu \cos t. \tag{26}$$

The unforced Duffing system (i.e., $\mu = 0$) is an example of an oscillator in a double-well potential. It has two coexisting fixed-point attractors corresponding to the two minima of the potential energy. For small μ, the forced Duffing oscillator has two attracting periodic orbits with the period of the forcing (i.e., 2π), one in each well of the potential. At $\mu = \mu_* \approx 0.2446$, a new attracting periodic orbit of period 6π arises through a saddle-node bifurcation. In Ref. [21], it is argued numerically that for a certain range of $\mu > \mu_*$ the basin of attraction of the 6π periodic orbit and the basins of attraction of the 2π periodic orbits have the Wada property. Thus, as μ decreases through the critical value μ_*, the period-6π attractor is destroyed via a saddle-node bifurcation on the fractal boundary of the basins of the other two attractors. This is an example of an indeterminate saddle-node bifurcation of the Duffing system which we study by considering the two-dimensional map in the $(\dot{x}, x)$ plane resulting from a Poincaré section at constant phase of the forcing signal. We consider orbits starting in the vicinity of the period-3 fixed-point attractor, and as we integrate the Duffing system, we decrease μ from $\mu_s > \mu_*$ to $\mu_f < \mu_*$ at a small rate of $\delta\mu$ per one period of the forcing signal. As μ approaches μ_* (with $\mu > \mu_*$), the period-3 fixed-point attractor of the unswept Duffing system approaches its basin boundary, and the slowly swept orbit closely follows its location. For $\mu - \mu_* < 0$ small, the orbit will approximately follow the one-dimensional unstable manifold of the $\mu = \mu_*$ period-3 saddle-node pair. Thus, we can describe the sweeping through the indeterminate bifurcation of the Duffing oscillator by the theory we developed for one-dimensional discrete maps. Figure 15 shows the final destination graph of a swept orbit initially situated in the vicinity of the period-3 fixed point of the Poincaré map. The final attracting state is represented as a 1 if situated in the potential well where $x > 0$ and
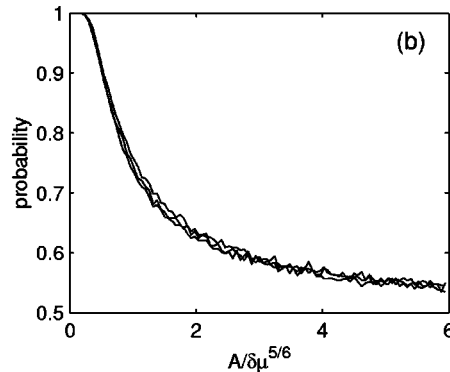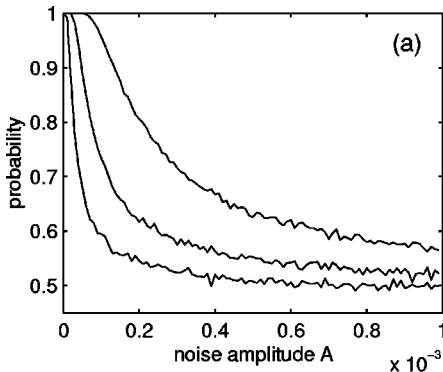

FIG. 16. Probability the Duffing oscillator reaches the attracting periodic orbit in the potential well at $x > 0$ for three values of $\delta\mu$ spread over one decade: (a) versus the noise amplitude A and (b) versus $A/(\delta\mu)^{5/6}$. We have chosen $\mu_s = 0.253$. From right to left, the $\delta\mu$ values corresponding to the curves are approximately $4.628\,716 \times 10^{-5}$, $1.461\,574 \times 10^{-5}$, and $4.621\,737 \times 10^{-6}$.
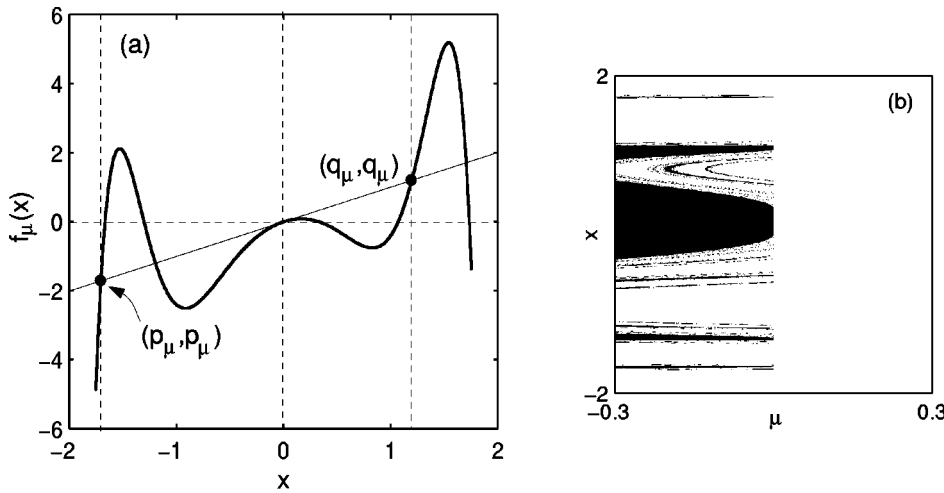
FIG. 17. (a) Graph of $f_\mu(x)$ versus x at the bifurcation parameter. (b) Basin structure of map $f_\mu(x)$ versus the parameter μ. The basin of attraction of the stable fixed point created by the saddle-node bifurcation is black while the basin of attraction of minus infinity is left white.

is represented as a 0 if situated in the potential well where $x<0$. As expected, the structure in Fig. 15 appears asymptotically periodic if graphed versus $1/\delta\mu$. In addition to slowly sweeping the Duffing system, consider an additive noise term $A\epsilon(t)$ on the right-hand side of Eq. (26), where on every time step $\epsilon(t)$ is chosen randomly in $[-1,1]$ and the time step used is $\Delta t=2\pi/500$. Figure 16(a) shows the dependence of the probability of approaching the attractor represented as a 1 versus the noise amplitude A for three specially selected values of $\delta\mu$ (centers of white bands in the structure of Fig. 15 where the swept orbit reaches the attracting state represented by 1) spread over one decade. Figure 16(b) shows collapse of the data in Fig. 16(a) to a single curve when the noise amplitude A is rescaled by $(\delta\mu)^{5/6}$, as predicted by our previous one-dimensional analysis (Sec. II F). Thus, we believe that the scaling properties of the indeterminate saddle-node bifurcation we found in one-dimensional discrete maps are also shared by higher-dimensional flows.

IV. INDETERMINACY IN HOW AN ATTRACTOR IS APPROACHED

In this section we consider the case of a one-dimensional map f_μ having two attractors A and B, one of which (i.e., A) exists for all $\mu\in[\mu_s,\mu_f]$. The other (i.e., B) is a node which is destroyed by a saddle-node bifurcation on the boundary between the basins of A and B, as μ increases through μ_* ($\mu_*\in[\mu_s,\mu_f]$). When an orbit is initially on B and μ is slowly increased through μ_*, the orbit will always go to A (which is the only attractor for $\mu>\mu_*$). However, it is possible to distinguish between two (or more) different ways of approaching A. [In particular, we are interested in ways of approach that can be distinguished in a coordinate-free (i.e., invariant) manner.] As we show in this section, the way in which A is approached can be indeterminate. In this case, the indeterminacy is connected with the existence of an invariant nonattracting Cantor set (a chaotic repeller) embedded in the basin of A for $\mu>\mu_*$.
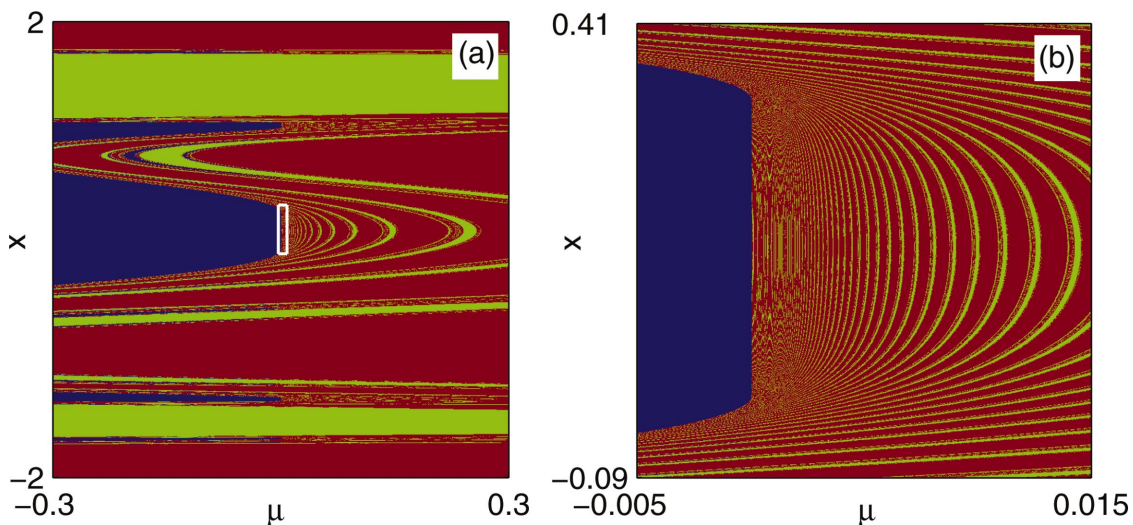

FIG. 18. (Color) (a) Basin structure of f_μ versus μ. We split the basin of attraction of minus infinity into two components: one plotted as the green region and the other plotted as the red region. The green region is the collection of all points that go to minus infinity and have at least one iterate bigger than the unstable fixed point q_μ. The red set is the region of all the other points that go to minus infinity. (b) Detail of Fig. 15(a) in the region shown as the white rectangle.
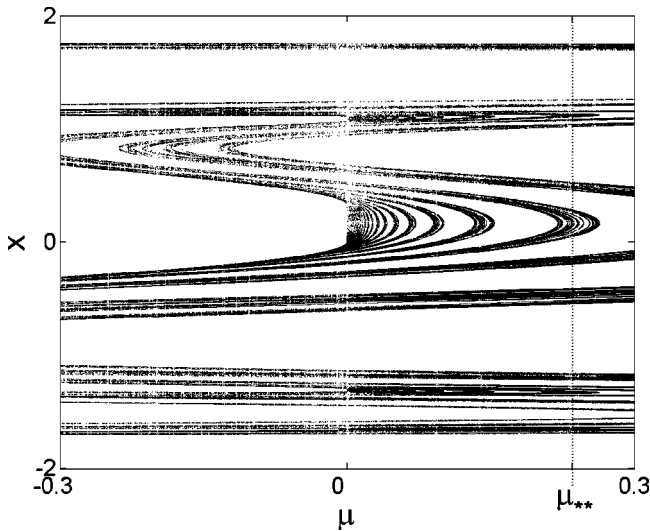
FIG. 19. The chaotic repeller of f_μ versus μ generated by the PIM-triple method. μ_{**} is an approximate parameter value where an indeterminate saddle-node bifurcation of a periodic orbit takes place; see Fig. 20.

As an illustration, we construct the following model:

$$f_\mu(x) = -\mu + x - 3x^2 - x^4 + 3.6x^6 - x^8. \tag{27}$$

Calculations show that f_μ satisfies all the requirements of the saddle-node bifurcation theorem for undergoing a backward saddle-node bifurcation at $x_* = 0$ and $\mu_* = 0$. Figure 17(a) shows the graph of f_μ versus x at $\mu = \mu_*$. Figure 17(b) shows how the basin structure of the map f_μ varies with the parameter μ. For positive values of μ, f_μ has only one at-

tractor which is at minus infinity. The basin of this attractor is the whole real axis. As μ decreases through $\mu_* = 0$, a new fixed-point attractor is created at $x_* = 0$. The basin of attraction of this fixed point has infinitely many disjoint intervals displaying fractal features [indicated in black in Fig. 17(b)]. This is similar to the blue basin $B[\mu]$ of the attractor B_μ of the previous one-dimensional model (see Sec. II A).

The blue region in Fig. 18(a) is the basin of attraction of the stable fixed point destroyed as μ increases through μ_*. For every value of μ we consider, the map f_μ has invariant Cantor sets. The trajectories of points which are located on an invariant Cantor set do not diverge to infinity. One way to display such Cantor sets is to select uniquely defined intervals whose end points are on the Cantor set. For example, Fig. 18(a) shows green and red regions. For every fixed parameter value μ, the collection of points that are boundary points of the red and green regions constitutes an invariant Cantor set. In order to describe these green and red regions we introduce the following notation. For each parameter value μ, let p_μ be the leftmost fixed point of f_μ [see Fig. 17(a)]. For every $x_0 < p_\mu$, the sequence of iterates $\{x_n = f_\mu^{[n]}(x_0)\}$ is decreasing and diverges to minus infinity. For each value of μ, let q_μ be the fixed point of f_μ to the right of $x = 0$ at which $(\partial f_\mu / \partial x)(q_\mu) > 1$. A point $(x; \mu)$ is colored green if its trajectory diverges to minus infinity and it passes through the interval (q_μ, ∞), and it is colored red if its trajectory diverges to minus infinity and it does not pass through the interval (q_μ, ∞). Denote the collection of points $(x; \mu)$ that are colored green by $G[\mu]$ and the collection of points $(x; \mu)$ that are colored red by $R[\mu]$. Using the methods and techniques of [22], it can be shown that the collection of points $(x; \mu)$ which are common boundary points of
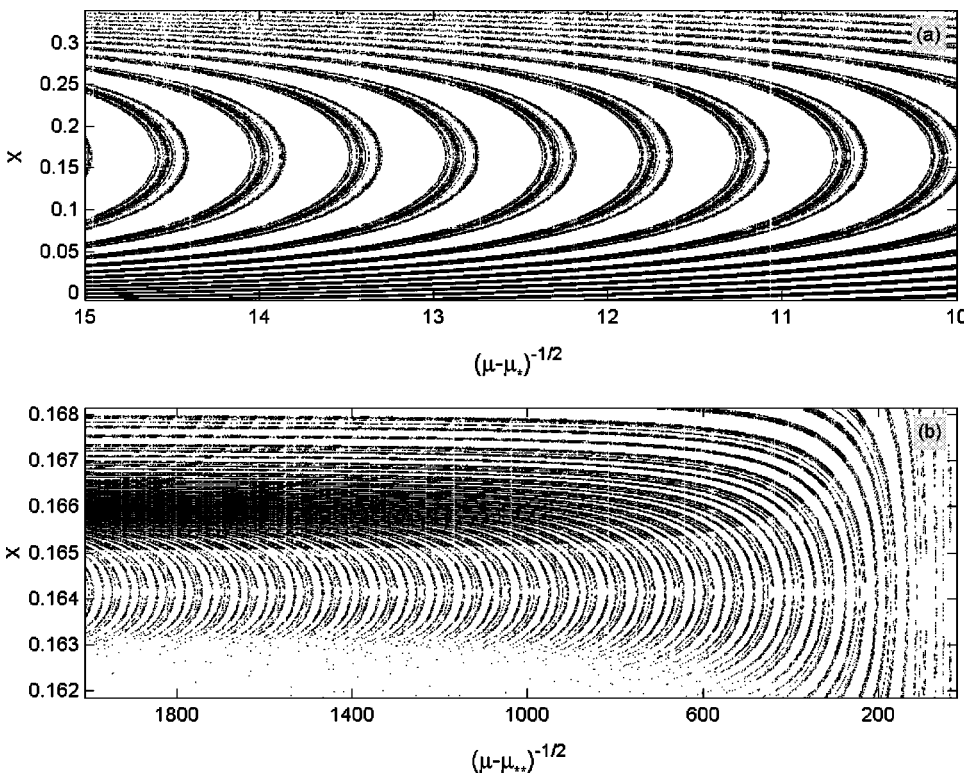

FIG. 20. The chaotic repeller of the map f_μ in the vicinity of the saddle-node bifurcation with the horizontal axis rescaled (from μ to) (a) $(\mu - \mu_*)^{-1/2}$ (notice that the chaotic repeller becomes asymptotically periodic) and (b) $(\mu - \mu_{**})^{-1/2}$, where $\mu_{**} = 0.234\,953\,84$. We believe that μ_{**} corresponds to the approximate value of the parameter μ where a saddle-node bifurcation of a periodic orbit of f_μ takes place on the Cantor set $C[\mu]$. In this case, the chaotic repeller also becomes asymptotically periodic.

$G[\mu]$ and $R[\mu]$ is a Cantor set $C[\mu]$ [23]. In particular, the results of [22] imply that for $\mu = \mu_* = 0$ the point $x_* = 0$ belongs to the invariant Cantor set $C[\mu_*]$.

Figure 18(b) is a close-up of Fig. 18(a) in the region of the saddle-node bifurcation. For values of $\mu > \mu_*$, in the vicinity of $(x_*;\mu_*)$, one notices a fractal alternation of red and green stripes. The green and red stripe structure in Fig. 18(b) shares qualitative properties with the structure in Fig. 2(b). All the analysis in Sec. II can be adapted straightforwardly to fit this situation.

Figure 19 shows how the chaotic repeller of the map f_μ, $C[\mu]$, varies with μ. The chaotic repeller is generated numerically using the proper interior maximum (PIM)-triple method. For an explanation of this method see Nusse and Yorke [24]. Using arguments similar to those in Sec. II C, we predict that changing the horizontal axis of Fig. 19 from μ to $(\mu - \mu_*)^{-1/2}$ makes the chaotic repeller asymptotically periodic. Numerical results confirming this are presented in Fig. 20(a). For f_μ given by Eq. (27), we were able to find a parameter value $\mu_{**} = 0.234\,953\,84$ (see Fig. 19) where changing the horizontal axis of Fig. 19 from μ to $(\mu - \mu_{**})^{-1/2}$ [see Fig. 20(b)] apparently makes the chaotic repeller asymptotically periodic [with a different period than that of Fig. 20(a)]. As in the case discussed in Sec. II, past the saddle-node bifurcation of f_μ at μ_*, infinitely many other saddle-node bifurcations of periodic orbits take place on the invariant Cantor set $C[\mu]$. We believe that μ_{**} is an approximate value of μ where such a saddle-node of a periodic orbit takes place.

V. DISCUSSION AND CONCLUSIONS

In this paper, we have investigated scaling properties of saddle-node bifurcations that occur on fractal basin bound-aries. Such situations are known to be indeterminate in the sense that it is difficult to predict the eventual fate of an orbit that tracks the prebifurcation node attractor as the system parameter is swept through the bifurcation. We have first analyzed the case of one-dimensional discrete maps. Using the normal form of the saddle-node bifurcation and general properties of fractal basin boundaries, we established the following universal (i.e., model independent) scaling results: (i) scaling of the fractal basin boundary of the static (i.e., un-swept) system near the saddle-node bifurcation, (ii) the scaling dependence of the orbit's final destination with the inverse of the sweeping rate, (iii) the time it takes for an attractor to capture a swept orbit scales with the $-1/3$ power of the sweeping rate, and (iv) scaling of the effect of noise on the capture probability of an attractor with the $5/6$ power of the sweeping rate. All these results were demonstrated numerically for a one-dimensional map example.

Following our one-dimensional investigations, we have explained and demonstrated numerically that these new results also apply to two-dimensional maps. Our numerical example was a two-dimensional map that results from a Poincaré section of the forced Duffing oscillator. In the last section of the paper, we have discussed how the new results listed above apply to the case where a saddle-node bifurcation occurs on an invariant Cantor set which is embedded in a basin of attraction, and we have supported our discussion by numerics.

[1] S.W. McDonald, C. Grebogi, E. Ott, and J.A. Yorke, Physica D **17**, 125 (1985).

[2] E. Ott, *Chaos in Dynamical Systems*, 2nd ed. (Cambridge University Press, Cambridge, England, 2002).

[3] L.N. Virgin, *Introduction to Experimental Nonlinear Dynamics* (Cambridge University Press, Cambridge, England, 2000).

[4] J.M.T. Thompson and M.S. Soliman, Proc. R. Soc. London, Ser. A **432**, 101 (1991); M.S. Soliman and J.M.T. Thompson, *ibid.* **438**, 511 (1992); J.M.T. Thompson, Physica D **58**, 260 (1992); M.S. Soliman, Proc. R. Soc. London, Ser. A **451**, 471 (1995).

[5] C. Baesens, Physica D **53**, 319 (1991); in *Dynamic Bifurcations*, edited by E. Benoît, Lecture Notes in Mathematics Vol. 1493 (Springer-Verlag, Berlin, 1991), p. 105; H.G. Davies and K. Rangavalhula, Proc. R. Soc. London, Ser. A **453**, 2043 (1997).

[6] N. Berglund and B. Gentz, Probab. Theory Relat. Fields **122**, 341 (2002).

[7] N.R. Lebovitz and A.I. Pesci, SIAM (Soc. Ind. Appl. Math.) J. Appl. Math. **55**, 1117 (1995).

[8] J. Guckenheimer, Invent. Math. **39**, 165 (1977); D. Whitley, Bull London Math. Soc. **15**, 177 (1983); Y.A. Kuznetsov, *Elements of Applied Bifurcation Theory*, Applied Mathematical Sciences Vol. 112 (Springer-Verlag, Berlin, 1995).

[9] Y. Pomeau and P. Manneville, Commun. Math. Phys. **74**, 189 (1980).

[10] J.-H. Cho, M.-S. Ko, Y.-J. Park, and C.-M. Kim, Phys. Rev. E **65**, 036222 (2002); C.-M. Kim, O.J. Kwon, E.K. Lee, and H. Lee, Phys. Rev. Lett. **73**, 525 (1994).

[11] H.E. Nusse, E. Ott, and J.A. Yorke, Phys. Rev. Lett. **75**(13), 2482 (1995).

[12] R. Breban, H.E. Nusse, and E. Ott, Phys. Lett. A **319**, 79 (2003).

[13] J. Kennedy and J.A. Yorke, Physica D **51**, 213 (1991); H.E. Nusse and J.A. Yorke, *ibid.* **90**, 242 (1996); Science **271**, 1376 (1996); Ergod. Theory Dyn. Syst. **17**, 463 (1997).

[14] C. Robert, K.T. Alligood, E. Ott, and J.A. Yorke, Physica D **144**, 44 (2000).

[15] B.-S. Park, C. Grebogi, E. Ott, and J.A. Yorke, Phys. Rev. A **40**, 1576 (1989).

[16] M. Misiurewicz and A.L. Kawczynski, Commun. Math. Phys. **131**, 605 (1990).

[17] H.E. Nusse and J.A. Yorke, Commun. Math. Phys. **150**, 1 (1992).

[18] J. Palis and M. Viana, in *Dynamical Systems*, edited by R. Bamón, R. Labarca, and J. Palis, Lecture Notes in Mathematics Vol. 1331 (Springer-Verlag, Berlin, 1988), p. 150; F. Takens, *ibid.* p. 196.

[19] *Handbook of Mathematical Functions with Formulas*, *Graphs*, *and Mathematical Tables*, edited by Milton Abramowitz and Irene A. Stegun (U.S. GPO, Washington, D.C., 1970).

[20] For numerical purposes, we consider that a swept orbit has reached its final state if $|x_{n+1} - x_n| < 10 \delta \mu$. Changing the factor of 10 to other values ranging from 1 to 30 can slightly change the numerical result for the slope (by as much as 3%).

[21] J. Aguirre and M.A.F. Sanjuán, Physica D **171**, 41 (2002).

[22] H.E. Nusse, SIAM (Soc. Ind. Appl. Math.) J. Appl. Math. **47**, 498 (1987).

[23] For every μ $(-0.3 < \mu < 0.3)$, write $p_\mu^* = \max\{x \in \mathbb{R} : f_\mu(x)$

$= p_\mu\}$ and $q_\mu^* = \max\{x \in \mathbb{R} : f_\mu(x) = q_\mu\}$. The interval $[q_\mu, q_\mu^*]$ also contains a Cantor set. By coloring this whole segment green, this information is lost. Therefore, the coloring scheme should be adapted if one wants to have the whole invariant Cantor set represented for every μ. For example, if a trajectory that diverges to minus infinity contains a point that is greater than p_μ^*, then the initial point is colored green; if a trajectory that diverges to minus infinity contains a point that is greater than q_μ^* but not greater than p_μ^*, then the initial point is colored yellow. A point is colored red if its trajectory diverges to minus infinity and does not have a point that is greater than q_μ^*. Then the collection of boundary points (a point x is a boundary point if every open neighborhood of x contains points of at least two different colors) is a Cantor set that contains the Cantor set described above.

[24] H.E. Nusse and J.A. Yorke, Physica D **36**, 137 (1989).